# Defect-enriched tunability of electronic and charge-carrier transport characteristics of 2D Borocarbonitride (BCN) monolayers from ab initio calculations

| | |
|---|---|
| Journal: | *Nanoscale* |
| Manuscript ID | NR-ART-05-2019-004096.R2 |
| Article Type: | Paper |
| Date Submitted by the Author: | 19-Jul-2019 |
| Complete List of Authors: | Yadav, Vivek; Temple University, Chemistry<br>Chakraborty, Himanshu; Temple University, Institute of Computational Molecular Science; Akashratna 401<br>Klein, Michael; Temple University<br>Waghmare, Umesh; Jawaharlal Nehru Centre for Advanced Scientific Research, Theoretical Sciences Unit<br>Ramachandra Rao, Chintamani; Jawaharlal Nehru Centre for Advanced Scientific Research, Chemistry and Physics of Materials Unit |
| | |

SCHOLARONE™
Manuscripts

# Defect-enriched tunability of electronic and charge-carrier transport characteristics of 2D Borocarbonitride (BCN) monolayers from ab initio calculations

Vivek K. Yadav$^a$, Himanshu Chakraborty$^a$, Michael L. Klein$^{a,*}$, Umesh V. Waghmare$^b$, C.N.R. Rao$^c$

a. Department of Chemistry and Institute for Computational Molecular Science (ICMS), Temple University, Philadelphia, USA 19122
b. Theoretical Sciences Unit, Jawaharlal Nehru Centre for Advanced Scientific Research, P.O Jakkur, Bangalore 560064, India
c. International Center for Materials Science, Jawaharlal Nehru Centre for Advanced Scientific Research, P.O Jakkur, Bangalore 560064, India

*Development of inexpensive and efficient photo and electrocatalysts is vital for clean energy applications. Electronic and structural properties can be tuned by the introduction of defects to achieve the desirable electrocatalytic activity. Using first-principles molecular dynamics simulations, the structural, dynamical, and electronic properties of 2D borocarbonitride (h-BCN) sheets have been investigated, highlighting how anti-site defects in B and N doped graphene significantly influence the bandgap, and thereby open up new avenues to tune the chemical behavior of the 2D sheets. In the present work, all of the monolayers investigated display direct bandgaps, which reduce from 0.99 eV to 0.24 eV with increasing number of anti-site defects. The present results for the electronic structure and findings for bandgap engineering open up applications of BCN monolayers in optoelectronic devices and solar cells. The influence of the anti-site distribution of B and N atoms on the ultra-high hole/electron mobility and conductivity are discussed based on density functional theory coupled with the Boltzmann transport equation. The BCN defect monolayer is predicted to have carrier mobilities three times higher than the pristine sheet. The present results demonstrate that BN doped graphene monolayers are likely to be useful in the next-generation 2D Field-Effect Transistor.*

**Keywords:** Borocarbonitride (BCN), Hole/Electron mobility, HER activity.

$^*$ *Corresponding author: E-mail: mlklein@temple.edu*

# Introduction

Graphene consists of a single atomic layer in which each carbon atom has $sp^2$ hybridization, resulting in a semi-metal or a zero-gap semiconductor. This monolayer 2D graphene sheet exhibits unusual property, which includes ultra-high charge carrier mobility ($10^5\,cm^2\,V^{-1}\,s^{-1}$), and thermal conductivity ($\sim 5000$ W/mK). This high carrier behavior adjusts when stacking graphene into bi or multilayer arrangements [1–3]. The fruitful utilization of graphene in various applications such as nano-electronic devices requires bandgap engineering, which in turn reduces its electron mobility [4–7]. Phenomena such as surface modification, or chemical doping with heteroatoms, creates a bandgap, and furthermore, this bandgap can be tuned accordingly. Doping with boron (electron-acceptor) or nitrogen (electron-donor) into graphene makes it a p-type or n-type material, respectively with the signature of finite bandgap [8–13]. Once the graphene is doped, it can be used as a supercapacitor [14], fuel cell [15], battery [16], and for water splitting[17] etc.

Doping of a heteroatom such as nitrogen (either pyrrolic, pyridinic or graphitic arrangement) in graphene can produce nitrogenated graphene [18–20]. The degree of doping is influenced by the concentration of the nitrogen source, temperature, and oxygen functionalities at the graphene edge. Later, graphene oxide (*GO*) gets simultaneously reduced, and nitrogen gets incorporated into the graphene lattice. For doping of boron in graphene, an approach similar to nitrogen doping has been employed [21,22]. Computational studies show that single atom nitrogen or boron doping in the graphene sheet produces a bandgap of $\sim 0.14$ eV [23,24]. This bandgap increases as the dopant concentration of boron or nitrogen in the graphene sheet increases. However, due to the electron-deficient and electron rich character of boron and nitrogen, the Fermi level shifts significantly by about 0.7 eV below and above the Dirac point, respectively. Apart from boron and nitrogen, graphene can also be doped with other heteroatoms such as sulphur, phosphorus, etc [25,26]. However, this work considers only the doping of graphene with boron and nitrogen.

The blend of both boron and nitrogen in a graphene sheet produces a new class of material having a small gap at the Dirac point, which exhibits new electronic structure properties, and possible applications. Borocarbonitrides ($B_x\,C_y\,N_z$) belongs to a family of exciting materials, which have better activity towards gas adsorption and catalytic properties. Using a thermal catalytic CVD method, B- and N-doped graphene (BCN) films can be synthesized, which have the potential for large-wafer growth of graphene [27–30]. Borocarbonitrides acquire high-surface area, and show excellent efficiency for supercapacitor applications [31]. Particularly, $B_1\,C_{4.5}\,N_1$ shows a specific capacitance of 178 and 240 in units of F/g in aqueous electrolyte and ionic liquids, respectively. This composition of BCN exhibits supercapacitor characteristics superior to nitrogen-doped graphene, or reduced graphene oxide [32]. The Oxygen reduction reaction (ORR) activity can be tuned by varying the carbon (C) to boron-nitride (BN) ratio. For sheets having a lower carbon concentration ($C < BN$), the conductivity is less than the sheet having a higher carbon concentration ($C > BN$)[33]. For example, $B_{12}C_{77}N_{11}$ shows an onset potential close to that of the commercial Pt/C catalyst, indicating an excellent ORR catalytic activity induced by the synergetic effect through co-doping with nitrogen and boron. CNR Rao and coworker demonstrated that BCN also, exhibits a remarkably high lithium cyclability and current rate capability [34]. The borocarbonitrides ($B_{15}\,C_{73}\,N_{12}$) prepared for this purpose possess high surface areas and exceptional stability and are likely to contain BCN rings as well as graphene and BN domains [32]. BN-doped graphene also exhibit good field emission properties similar to carbon nanotubes[35,36]. BN-doped carbon nanosheets are used for metal-free light-induced water splitting as it can catalyze hydrogen or oxygen evolution from water as well as carbon dioxide reduction under visible light illumination [37–41].

In the present work, ab initio calculations have been employed to detail structural, dynamical and electronic properties of the $B_{15}C_{90}N_{15}$ sheet with and without the lattice type defect as shown in **Figure 1**. Such defects can be engineered experimentally by electron irradiation. For example, Su and coworkers recently demonstrated controlled dynamics of phosphorus (P) dopants in graphene to a desired chemically ordered configuration using electron irradiation, supported by theoretical analysis of relative probabilities of possible configurations resulting from collision of electrons with P [42]. Defect follows (-BNNBBN-) whereas non-defect follows (-BNBNBN-) type of arrangement along the vertical direction, respectively (see **Figure 1**). All the nanosheets studied in this work have the same numbers of electrons. As mentioned above, this composition of BCN demonstrates higher surface area and exceptional stability compared to other closest analogs. This work is mainly emphasizing the defect-mediated tunability in the carrier transport and bandgap of $B_{15}C_{90}N_{15}$ sheets.

The paper is organized as follows. In the next section, computational details are presented for investigation of the carrier transport and electronic properties of different types of BN-doped graphene sheets. This is followed by a discussion of the results and a conclusion.

## Simulation Details

Born-Oppenheimer ab initio molecular dynamic (AIMD) simulations have been carried out using the CP2K/Quickstep package[43,44] at 300 K. It is important to remember that the Born- Oppenheimer approximation is only a good approximation if the relaxation time of the electronic structure is much faster than that of the movement of the nuclei. This approximation obviously ignores some important things, for example the momentum of electrons but that is typically small compared to the momentum of the nuclei and thus does not matter. In our study, density functional theory (DFT) was applied within generalized gradient approximation (GGA), using Perdew-Burke-Ernzerhof (PBE) functional[45]. The dispersion corrected scheme proposed by Grimme i.e. DFT- D3 [46,47] the basis set DZVP-MOLOPT-SR-GTH [48] optimized for calculating molecular properties in gas and condensed phase was applied for all atoms in the system. In addition, Gaussian and Plane-Wave (GPW)[49] method was used to reduce the computational cost. This method uses an atom-centered Gaussian-type basis to describe the wave functions and an auxiliary plane wave basis to describe the electron density. It is worth noting that only the valence electrons were explicitly treated. Their interaction with the remaining ions is described using the pseudopotentials of Goedecker-Teter-Hutter (GTH)[50,51]. The charge density cutoff of the finest grid level is equal to 400 Ry. Both (for defect and non- defect system) simulations were carried out in the NVE ensemble with a timestep of 0.5 fs. The temperature was set to constant 300 K using a canonical sampling through velocity rescaling (CSVR) thermostat. Statistics were collected after thermal equilibration. The studied system consisted of a single boron-nitrogen-graphene sheet represented by 120 atoms out of which 90 belongs to carbon and 15 each of boron and nitrogen. The evolution of kinetic energy and potential energy during the 60 ps trajectory is shown in **Figure SI-1** of supporting information.

We have also performed density functional theory calculations for a series of h-BCN sheets with and without defects using the PWscf package of the Quantum Espresso[52] distribution. The ultrasoft pseudopotentials of Rappe-Rabe-Kaxiras-Joannopoulos (rrkjus) [53] were used to describe the core electrons for all the atomic species. To consider the electron exchange and correlation potential, the Perdew-Burke-Ernzerhof[45] formulation of the generalized gradient approximation (GGA) was chosen. A 680 eV (50 Ry) kinetic energy cutoff for the plane-wave basis set and 5440 eV (400 Ry) for the charge density was used, obtaining an accuracy of $10^{-8}$ eV in the self-consistent calculation of the total energy, using a converged Monkhorst-Pack k-point grids[54] of 10 X 10 X 1. The positions of the atoms in the unit cell were relaxed toward equilibrium until the Hellmann Feynman forces became less than 0.001 eV/A. The supercell approach with periodicity in x and y directions was implemented. Vacuum space of 20 Å was used in the z-direction to nullify the interaction of the sheet with its periodic images and in addition to assure the elimination of the coupling between them. The van der Waals correction proposed by Grimme (D3 correction) [46,47] was employed in this work. Phonon dispersion curves for BCN (in **Figure 1**a) were computed by employing density functional perturbation theory (DFPT)[55] to obtain dynamical matrix on a mesh of 3 X 3 X 1. These were Fourier interpolated to obtain dynamical matrices and phonon spectra at arbitrary wave vector q. This method avoids using a supercell approach and allows the calculation of the dynamical matrix at arbitrary q-points. We performed this phonon calculation on a twenty-four atoms unit cell.

The semi-classical Boltzmann equation, under the constant relaxation approximation, was implemented using the Boltztrap code [56] to compute to carrier mobility. A highly dense k-mesh of 20 X 20 X 1 (for scf) and 40 X 40 X 1 (for nscf) were used for transport property calculation. Indeed, the constant relaxation time approximation has been widely used in the theoretical calculations of thermoelectric materials and has successfully predicted the temperature and carrier concentration dependence of the transport properties. Besides, we also used Deformation potential theory[59,60] to calculate the electron and hole mobility separately and the results were compared with Boltzmann theory.

## Results and Discussion

### ab initio molecular dynamics

Our results in this section are based on the 60 ps ab initio trajectory generated for both BCN and BCN-defect as displayed in **Figure 1**a and **1**b, respectively. In **Figure 2**, we show the pair correlation between (a) Boron (B)-Boron (B), (b) Boron (B)-Nitrogen (N), and (c) Nitrogen (N)-Nitrogen (N), respectively. With the inclusion of defects in the sheet, an additional B-B peak appears at 3.8Å due to the flip in the position of boron with nitrogen shown in **Figure 2**(a). In the same plot, the splitting of the B-B peak occurs at 4.95Å with an additional shoulder at 5.12Å also results from the defect in the BCN sheet. Similarly, **Figure 2**(b) and **Figure 2**(c), shows the splitting of peaks in the third coordination shell because of the flip in the position of the boron and nitrogen. We also computed the pair correlation between the carbon atoms in the sheet (results shown in SI-2). The first, second, and third coordination shell carbon-carbon peaks appears at 1.41Å, 2.47Å, and 2.87Å, respectively. The experimentally measured average C-C bond length in single-crystalline regions of single-layered graphene by transmission electron microscopy is 1.42 ± 0.05Å [62,63] . The pair correlation between the carbon with boron, nitrogen, and carbon is shown in **Figure S2** of supporting information. The velocity autocorrelation function (VACF) for both the monolayers are presented in **Figure 3**a. We found similar qualitative behavior of VACF in both the sheets, with an envelope relaxation time of less than 1 ps. Explicitly, the location of minima and maxima of the VACF are found to be similar for both the monolayers. The first minima of the VACF is observed at 12 fs indicating the corresponding back scattering time duration in both the monolayers. As expected, it was found that contribution of the VACF from in-plane (x/y) direction is distinct from the out-of-plane (z) direction (not shown here). The study on velocity distribution also explore the influence of defect on the fluctuation in the nanosheet. We computed the velocity distributions for the both the sheets along the simulation trajectory and plotted them in **Figure 3**b. The velocity distribution peak for BCN defect is slightly on the higher side compared to the BCN sheet. The mean value of velocity distribution for BCN is 7.06±2.99 Å/ps, whereas, for BCN-defect, it is found to be 7.41 ± 3.13 Å/ps. The results from VACF and velocity distribution shows that the inclusion of a defect in the sheet produces higher lattice vibrations compared to the pristine BCN monolayer. A comparison of the phonon density of states $D(\omega)$, of BCN and BCN-defect monolayer is presented in **Figure 4**. The plot shows total $D(\omega)$ (averaged over x, y, and z directions) for both the sheets. The most intense peak in the total $D(\omega)$ for the BCN-defect system is blue-shifted (higher frequency) with respect to that of the pristine BCN sheet. This is due to higher fluctuations in C, B, and N atomic positions induced by the defect in the sheet. The maximum of $D^{max}(\omega)$ peak frequency for BCN and BCN-defect are 40.96 and 42.94, in units of THz, respectively. In addition, we found that the D-band is sensitive to doping, and line width and frequency of this peak can be employed to check the doping level. The green arrow in **Figure 4** indicates the shift of peak from BCN to BCN- defect. We conclude from the VACF, velocity distribution, and PDOS that, presence of a defect in the BCN monolayer displays the signature of higher lattice vibrations, which also influences the various electronic properties discussed in the later section.

In order to calculate the linear IR spectrum from AIMD, information regarding the dipole moment of the sheets must be computed from the simulation trajectory. An efficient approach is to localize the molecular orbitals to obtain Wannier centers. In this fashion, we computed the IR spectra of the BCN sheets using the IR module of TRAVIS [64,65] software as shown in **Figure 5**. The maxima of the $D^{max}(\omega)$ peak appears at 41.78 and 41.69 for BCN and BCN- defect, in unit of THz, respectively. In IR spectra, the peak around 20 THz is missing, which is possibly due to less electronic contribution in the z-direction compared to the x-y plane. IR has contributions from phonons contributed due to elastic collisions whereas phonon density of states (PDOS) has both elastic and inelastic contributions including anharmonicity. The maximum of $D(\omega)$ peak for BCN and BCN-defect appears at equal position (with in error bar) as the total electron of the system is constant. The IR spectra is not influenced by the presence of defect apart from the shift in the peak height of the $D^{max}(\omega)$ as it depends on the distribution of the total number of electrons in the sheet.

**Carrier mobility**

An ideal candidate for optoelectronic devices is expected to simultaneously have an appropriate bandgap (for better light absorption) and a superior charge carrier transport ability. On the other hand, the power factor of electronic devices depends both on carrier transport properties and also on current conversion efficiency. Graphene (in single layer), popular electronic material, displays very high carrier mobility of ($\sim 10^5 cm^2 V^{-1} s^{-1} at 300K$), due to the presence of massless Dirac fermions. The presence of dopant B and N in this case, opens the bandgap, which satisfy both the criteria mentioned above. A deformation potential approximation (DPA)[59] method with the effective mass approximation has been employed to investigate carrier mobility (μ), which is expressed for 2D materials[61] as:

$$\mu = \frac{e\hbar^3 C_\beta^{2D}}{k_B T m*^2 E_1^2}$$

(1)

here $e$ is the charge of electron, $\hbar$ (= $h/2\pi$) and $h$ is Plank's constant, $k_B$ is Boltzmann constant, $C^{2D}{}_\beta$ is the elastic constant in direction (β= x- or y-axis) of applied strain, and T is temperature (300K in present case). The term $E_1$ is defined as deformation potential constant and expressed as $E_1 = \Delta V/(\Delta l/l_0)$. In this expression, $\Delta V$ represents the energy change under proper cell compression or dilation. The change of the conduction band minimum (CBM) is used for electrons and the valence band maximum (VBM) for holes. The deformation of the lattice length ($l_0$) is denoted as $\Delta l/l_0$ and is set to be -0.02, -0.015, 0.010, 0.05, 0.00, 0.05, 0.01, 0.015, 0.020. The effective mass ($m^*$) in the transport direction is computed by

$$m^* = \hbar^2 \left[\frac{\partial^2 E(k)}{\partial k^2}\right]^{-1}$$

(2)

where $k$ stands for wave vector and $E$ is the energy. The effective mass and deformation potential constant can be computed from the band structures, whereas the elastic modulus is extracted from phonon dispersion relations. The experimentally measured elastic constant $C^\beta$ for graphene is 350 $N/m$ and BN (260 $N/m$), which shows their strain induced stability [66–68]. The elastic constant for the present system is found to be ~316 $N/m$ for both cases, which is more than h-BN and less than graphene, as expected. The computed results show that BCN-defect system have ~ 3 times more hole/electron mobility compared with pristine BCN sheet. It is also worth to note that the value of hole/electron mobility along the y-axis is higher than the x-axis, which is possibly due to difference in the B-N arrangement. The results of various calculations such as deformation potential, elastic constant, hole/electron mobility along x-and y-axis of pristine and BCN-defect is given in **Table 1**. Details of parameters used in deformation potential theory are explained in SI-3(a-c).

Further, the semiclassical Boltzmann theory within constant relaxation time approximation using the BoltzTrap code[56] has been employed to compute the conductivity of BCN and BCN-defect system. Herein, the conductivity is calculated using the equation

$$\sigma_{\alpha,\beta}(T,\nu) = \Sigma_i \int \frac{dk}{8\pi} \left[-\frac{\partial f(T,\nu)}{\partial \varepsilon}\right] \sigma_{\alpha,\beta}(i,k)$$

(3)

where $f$ is the Fermi-Dirac distribution function and $\nu$ is the chemical potential that is determined by the number of free carriers. The term $\sigma_{\alpha,\beta}(i,k) = e^2 \tau_{i,k} \nu_\alpha(i,k) \nu_\beta(i,k)$ denotes the conductivity tensor, where $\nu(i,k) = \hbar^{-1} \partial \varepsilon_{i,k}/\partial k_\alpha$ represents the group velocity of $i$th band for the α component. The calculated conductivity (σ/τ) as a function of temperature using BoltzTrap code is shown in **Figure 6**. From the figure, it is clear that conductivity of BCND increase with temperature much earlier than the pristine BCN system. The conductivity of BCND at 300 K was found to be $1.50 \times 10^{16}$ whereas BCN has conductivity $2.50 \times 10^{10}$ at room temperature. The reason for higher conductivity in BCND at room temperature may be due to small bandgap (0.24 eV) in BCND compared to BCN, which has a bandgap of 0.99 eV ($\sim$ 4 times more than BCND). From this section, it is concluded that both Boltztrap and deformation potential theory predict the same higher carrier transport in the BCN-defect monolayer compared to the pristine sample.

**DFT based electronic calculations**

In electronic structure calculations of solids, the energy cutoff and the number of k-points in the Brillouin zone are two crucial parameters which need attention. A convergence study of the quantity of interest was performed with respect to these parameters prior to production runs. A cutoff of 50 Ry was employed, and for relaxation (scf) 5 X 5 X 1 (10 X 10 X 1) k-points shows better convergence of the total energy with respect to the energy cut-off and the number of k-points. To check the lattice dynamical stability of BCN monolayer, the phonon dispersion of BCN sheets (**Figure 1** a,b) were calculated and shown in **Figure SI-4**. It is evident that BCN monolayer displays dynamical stability as it has a positive frequency throughout the Brillouin zone. It is also noted that the BCN has a maximum frequency value of 1574 cm$^{-1}$, which is comparable to graphene[57]. The flexural modes exhibit quadratic dispersion at long wave-lengths, and have comparatively lower frequencies than those of the transverse and longitudinal acoustic modes. Similar results have been found for a $C_4N_4$ monolayer suggesting dynamic stability where all branches of the phonon spectrum are positive and no imaginary phonon mode exists [58]. For **Figure 1**, the cohesive energy is found to be 8.795 and 8.787 eV/atom for the BCN and BCN-defect, respectively. This cohesive energy is defined as

$$E_{coh} = \left( \sum E_{atom} - E_{monolayer} \right) / N \qquad (4)$$

where $E_{monolayer}$ is the total energy of the monolayer sheet, $E_{atom}$ the energy of the individual atoms, and $N$ is the total number of atoms in the unit cell. The total energy of the free atom has been obtained from a calculation at Γ point using the same energy cutoff as chosen for the monolayer. We also calculated the cohesive energy of the systems shown in **Figure 7** with different anti-site defects and given in **Table 2**. The results from $E_{coh}$ of various BCN-defect systems also show that all the systems are fairly stable as their computed cohesive energy is almost equal to pristine BCN sheet. To strengthen the present results, using the same level of theory, the cohesive energy for the pristine graphene and h-BN sheet was calculated and is found to be 9.153 and 8.735, in units of eV/atom, respectively. These results for cohesive energies of BCN sheets lie in between those for graphene and h-BN sheets.

A comparative analysis was performed of the energetic stability of structures with different defects, relative to **Figure 1**a using a zero-temperature thermodynamic approach based on the prior determination of the chemical potentials [69]. The chemical potential for a CC and BN pair is obtained from a carbon and boron-nitride infinite monolayer calculation performed at same level of theory, which results in μ$^{layer}_{CC}$= −310.20 $eV$, and μ$^{layer}_{BN}$ = −358.38 $eV$, respectively. The first-principles calculation results for the formation energy of various BCN monolayers are shown in **Table 2** using equation 5,

$$E_f = [E_{BCN} - (n_{CC} \mu_{CC} + n_{BN} \mu_{BN}] / N \qquad (5)$$

The pristine BCN system (**Figure 1**a), shows a bandgap $E_{gap}$ of 0.986 eV, whereas the maximum defect system (**Figure 1**b), displays a bandgap of 0.244 eV. As DFT-GGA (PBE) significantly underestimates the bandgap in materials, we performed an additional calculation using the HSE[70] functional as implemented in Quantum Espresso. Our estimates of bandgaps of pristine BCN and BCN defect monolayer (**Figure 1**) with HSC calculations are 1.53 and 0.83eV, respectively. We note that the PBE band-gaps are up to ∼ 50 % underestimated, as they typically are. Thus, these results predict tunable behavior of bandgap proportional to the numbers of anti-site defects in the BCN sheet. The **Figure 8** (a-c) shows bandgap, cohesive energy value for the systems shown in **Figures 1** and **7**. The computed values of Cohesive Energy, Formation Energy, HOMO and LUMO position, Bandgap for pristine BCN and various anti-site configurations of BCN sheet are shown in **Table 2**. The computed bandgap for pristine graphene and h-BN sheet are 0.012 and 4.295, in units of eV, respectively. However, the bandgap is underestimated in GGA, the actual value of the bandgap is expected to be larger and close to the value for silicon in some cases. Therefore, lattice type defects in BCN offers an interesting possibility for nanoelectronics with direct bandgap that has nearly the same value as in bulk silicon[71].

We have seen that all BCN systems are direct bandgap semi-conductors with the highest occupied crystalline orbitals (HOCOs or HOMO) and lowest unoccupied crystalline orbitals (LUCOs or LUMO) located between M and K point of the reciprocal space (see **SI-5**). However, the Fermi level is placed exactly in between the valence and conduction bands as there are no predominating charge carriers (either electrons or holes) in these hybrid systems. These systems can be considered as nanohybrids where the CC pairs are replaced by their isoelectronic analogue BN pairs, thereby inducing no extra charge carriers. Because C-C bonding is stronger than C-B and C-N bond, while the hexagonal configuration has more C-C bonds thus energetically more stable. Interestingly, the valence and conduction bands are symmetric with

respect to the Fermi energy due to the electron hole symmetry. From these calculations, we strongly propose a series of metal free materials with direct bandgap useful for optoelectronic devices.

## Work function and hydrogen evolution reaction

In materials, the work function ($\Phi$) can be defined as the energy required to eliminate an electron from the highest filled level in the Fermi distribution of a solid to vacuum at absolute zero temperature.

$$\Phi = E_{vac} - E_{fermi} \qquad (6)$$

where $E_{vac}$ is the vacuum level and $E_{fermi}$ is Fermi level. In the numerical calculations, $E_{fermi}$ is obtained by integrating the density of states from the lowest energy level to an energy level that gives the total number of electrons in the unit cell. $E_{vac}$ is determined using the planar-average electrostatic potential energy along the z-axis i.e. direction of box vacuum. Plots of the work function are shown in **Figure SI-6** of supporting information. Due to the isoelectronic nature of the BCN sheets used in present study, the computed value of $\Phi$ is ~4.13 eV for all the sheets irrespective of the BN pair arrangement or defect. The experimentally measured work function ($\Phi$) for graphene falls between 4.45-4.50 eV[72]. The ~ 9–10% decrease in the $\Phi$ for BCN sheets compared to pristine graphene is due to presence of BN pairs.

Hydrogen production through water splitting is a clean and environmentally benign energy source. The criteria for HER is that the band structure of the semiconductor must straddle the redox potential of water [73]. In order to support this claim, the band edge positions of pristine and defected BCN sheets are compared with the reduction potential of water ($H^+/H_2$). The band edge positions of valence and conduction bands were determined by aligning them relative to the vacuum potential obtained from calculation of the respective sheets using the equations, $E_{VBE/CBE} = E_{VBM/CBM} - E_{vac}$. For all the configurations of BCN in present study, Fermi energy ($E_{fermi}$) is around ~ -2.25 eV, which gives an overpotential of about 2.2 eV relative to the redox potential of HER. It is clear from **Figure 9** that the HER potential of water lies within the bandgap for first 3 configurations, which shows that BCN sheets have the ability to reduce $H^+ to H_2$ and provide new opportunities in the field of photocatalysis. The valence and conduction band edges of these three systems straddle the HER redox potential whereas others do not. Thus, it is concluded that the first three systems in **Figure 9** can be proposed as metal free electrocatalysts. Conduction and valence bands of BCN with maximal defects (**Figure 1**b) obtained from calculations based on the HSE functional, also straddle the redox potential of HER while the bandgap increases from 0.24 to 0.83 eV. We thus conclude that results of HSE functional based calculations suggest that electronic structure of all the BCN systems considered here is favorable to their HER activity. As BCN already shows potential to replace the Pt based electrocatalysts, so fine tuning in its bandgap by creating defect (by flipping the BN arrangement) will be helpful in preparation of efficient non-metal photo- and electro-catalysts for HER.

## Conclusions

In summary, a variable bandgap has been demonstrated in graphene by tuning the level of BN doping. In all cases studied, the bandgap is direct, which could lead to applications of hybrid graphene layers in optoelectronics and solar cells. A significant finding is that the bandgap depends upon the B-N pair arrangement in graphene in addition to the concentration and shape of BN patches. The present work regarding bandgap engineering should help to tailor the properties of such hybrid layers. Carrier mobility was found to be an order of $10^4 cm^2 V^{-1} s^1$ which is significantly larger than $MoS_2$ and Silicon[71,74–76]. The present findings on carrier transport also show the tunability of the ultra-high mobility by introduction of anti-site defects in the monolayer. The computed carrier mobility of the BCN sheets is consistent with the calculated bandgaps. The present findings pave the way for the potential functionality of h-BCN to be utilized as efficient photovoltaic devices. In the future, we propose to perform ab initio calculations using more reliable hybrid functionals[70,77], as GGA functionals such as PBE and BLYP underestimate the bandgap[78,79].
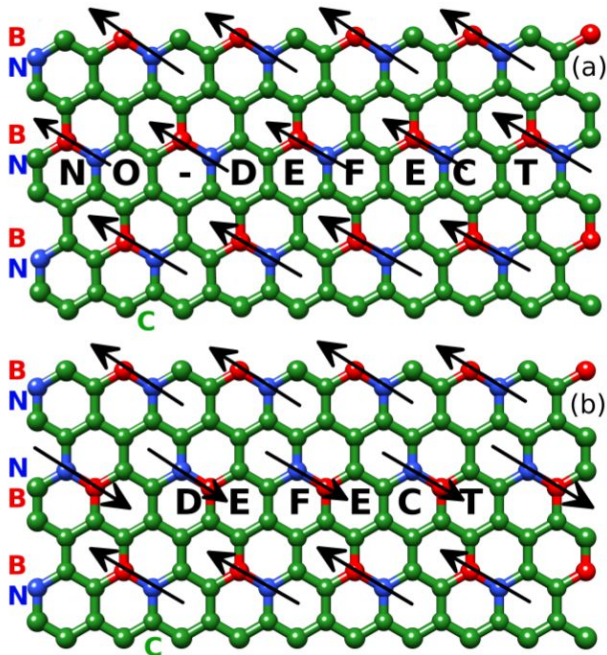
## Acknowledgment

**Fig. 1** BCN sheet with (a) no defect and (b) defects. A defect is defined as a flip in the position of a pair of B and N. and represented by down arrow.
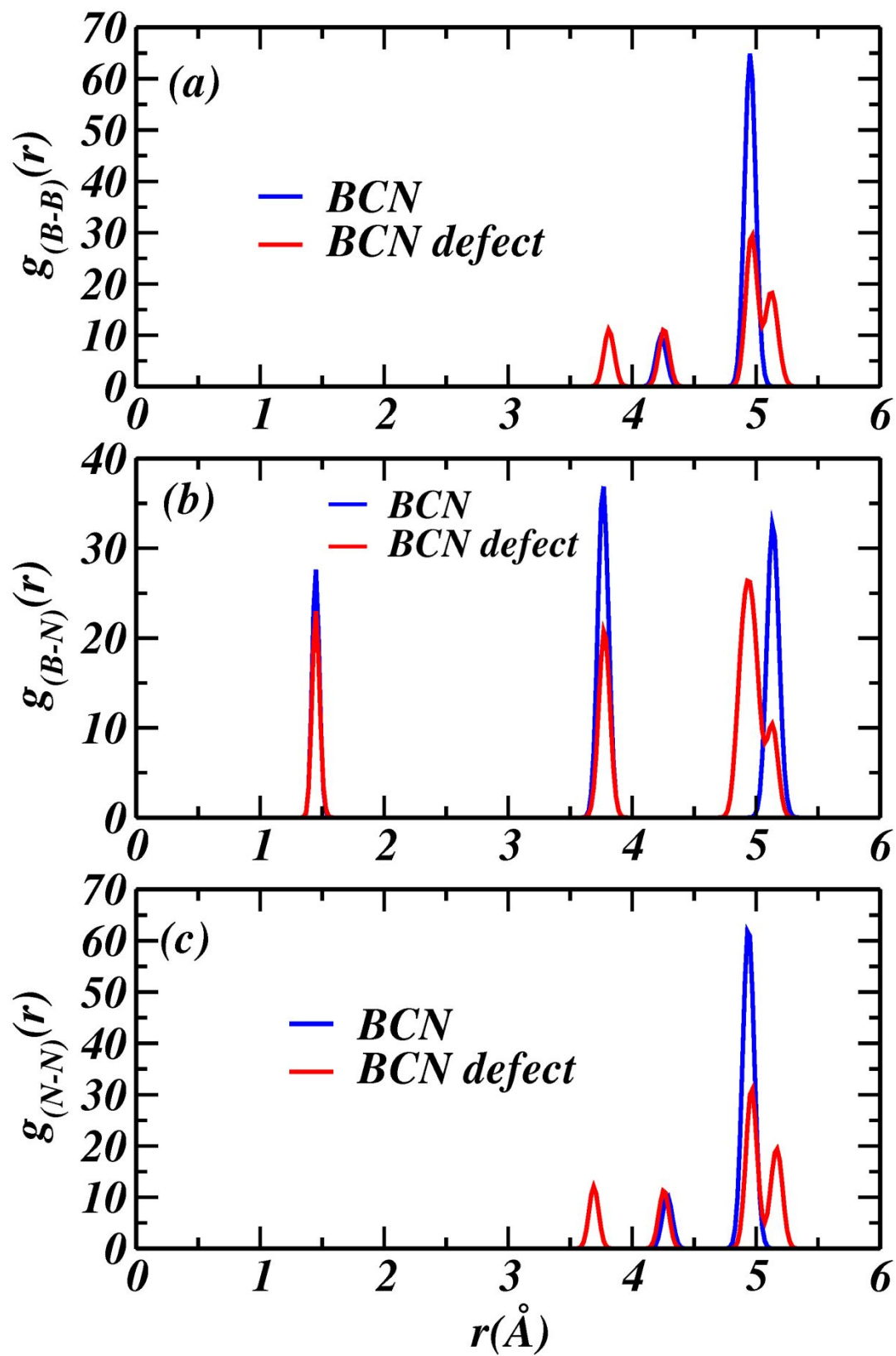
**Fig. 2** Pair correlation between (a) Boron (B)-Boron (B), (b) Boron (B)-Nitrogen (N), and (c) Nitrogen (N)-Nitrogen (N) pairs of atoms for BCN and BCN-defect configurations (Fig.1).
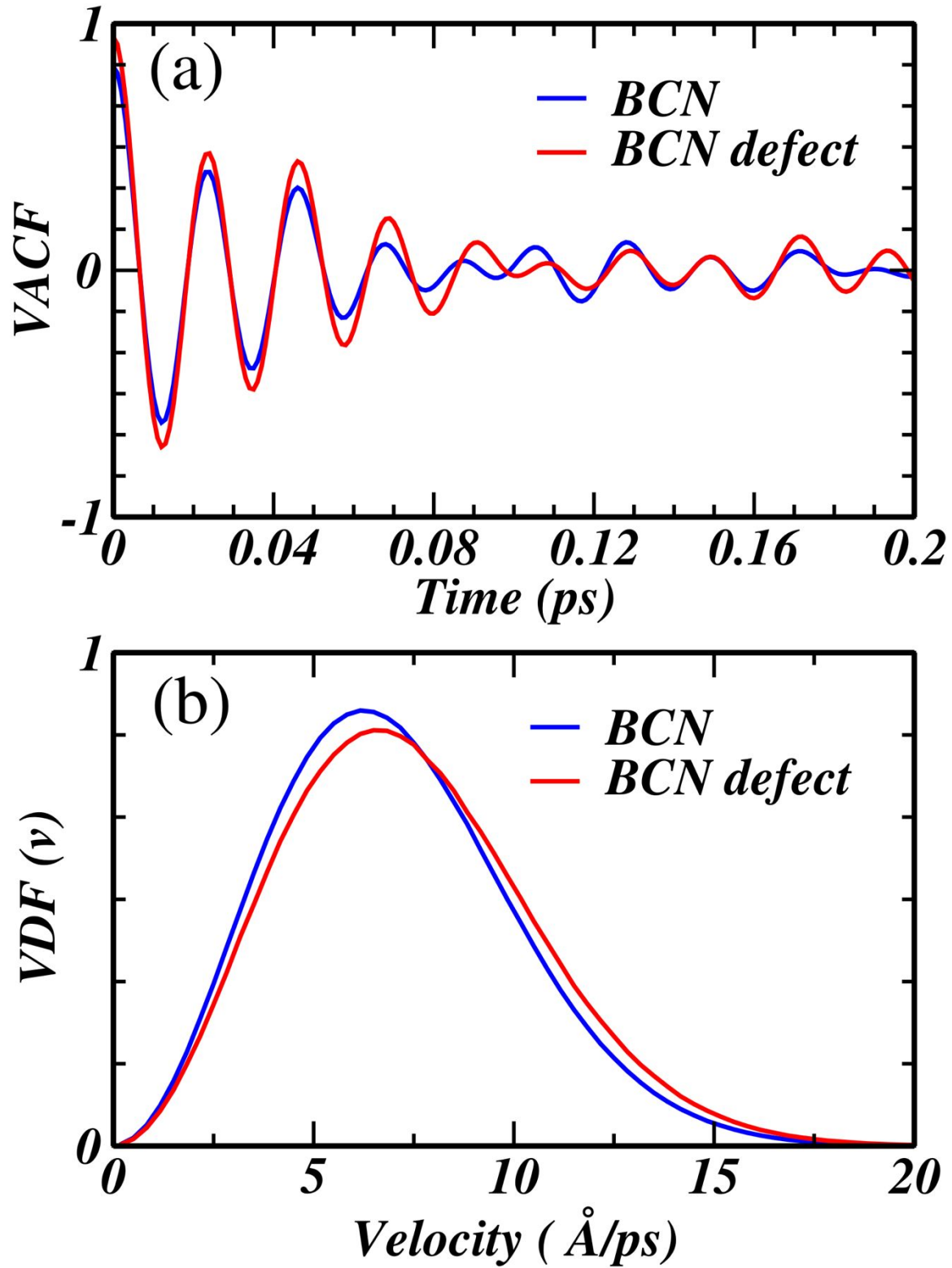
**Fig. 3** (a) Velocity autocorrelation function (VACF), and (b) Velocity distribution (VDF) function for BCN and BCN-defect configurations (Fig. 1).
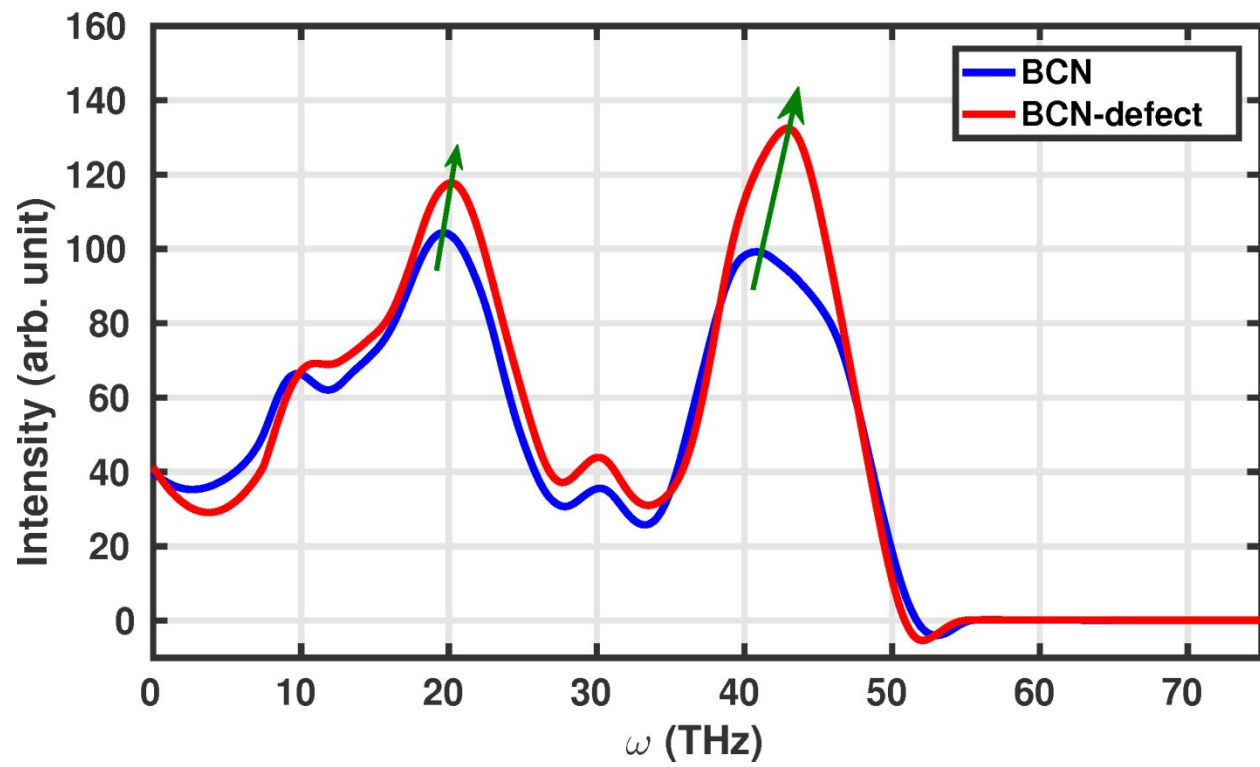
**Fig. 4** Phonon density of states (PDOS) of BCN and BCN-defect configurations (Fig. 1).
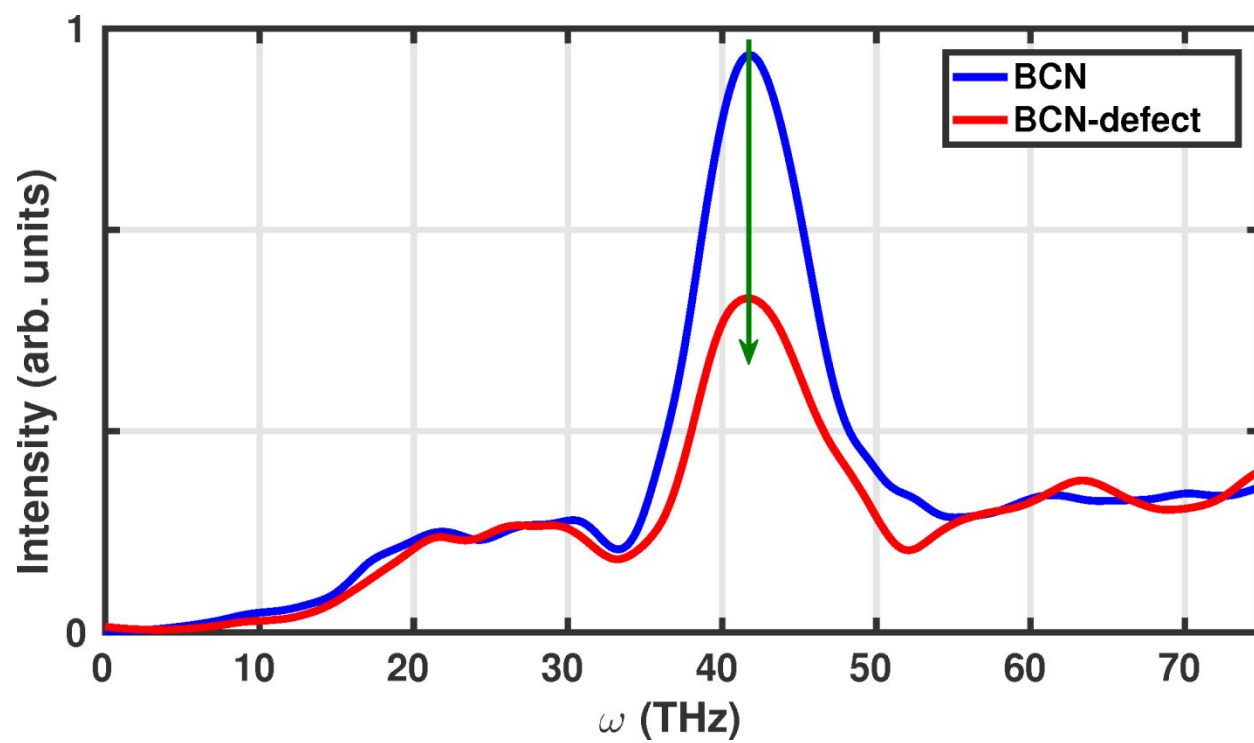
**Fig. 5** Infrared (IR) spectrum of BCN and BCN-defect configuration (Fig. 1).
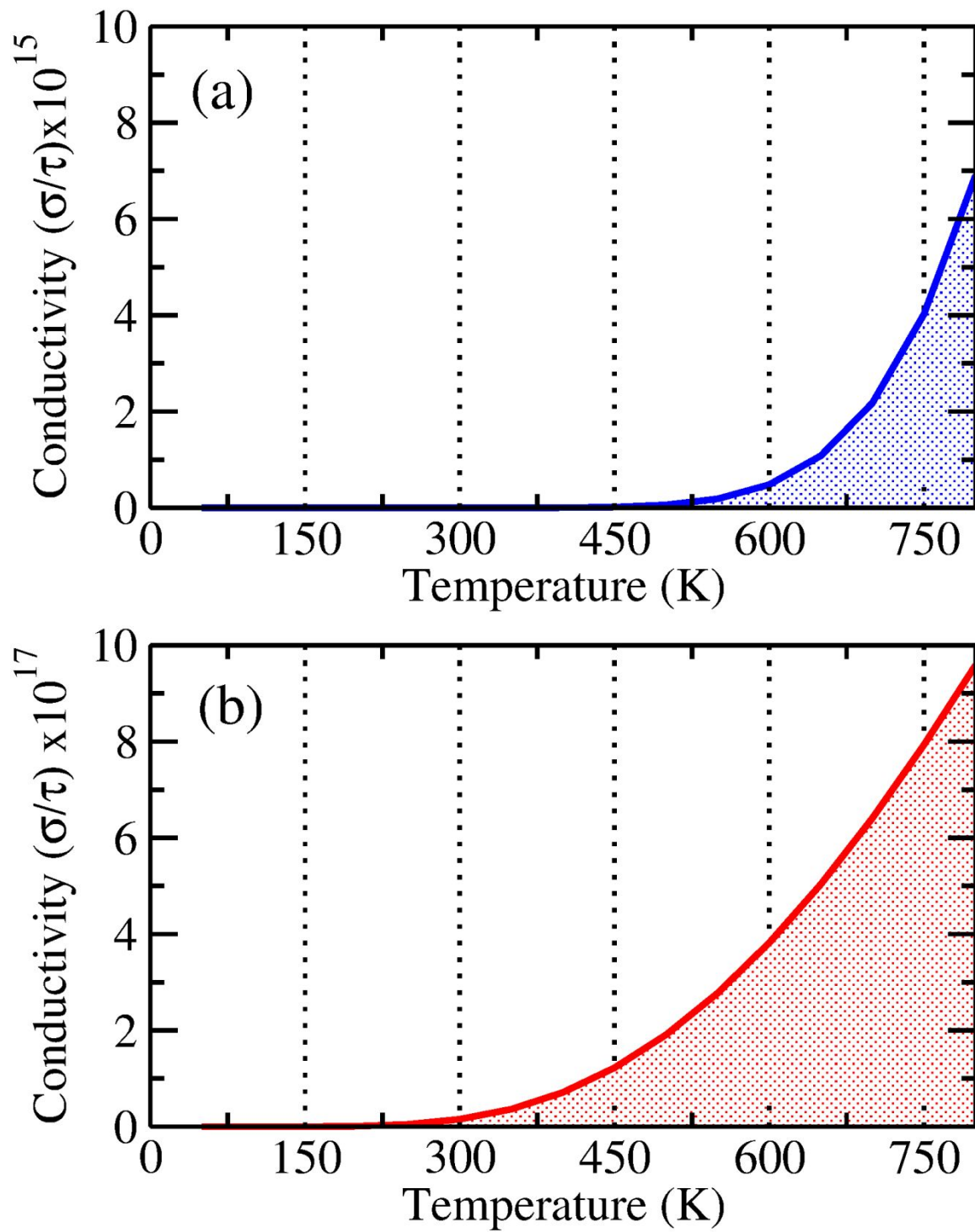
**Fig. 6** Conductivity in units of $(\Omega^{-1}\,cm^{-1}\,s^{-1})$ as a function of temperature for (a)BCN, and (b) BCN-defect configuration (Fig. 1).
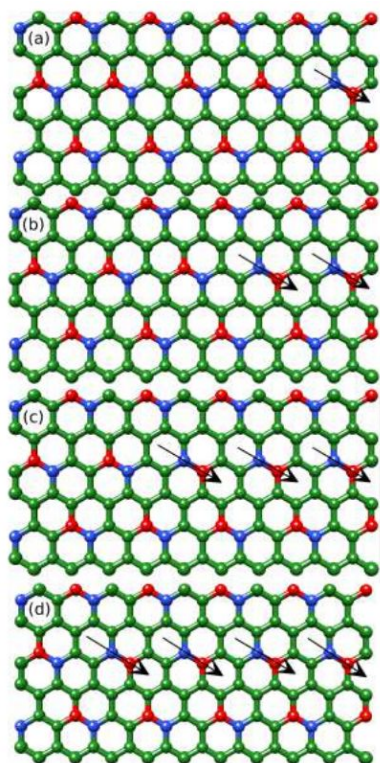
**Fig. 7** BCN sheet with defects involving (a) 1 pair of BN, (b) 2 pairs of BN, (c) 3 pairs of BN, and (d) 4 pairs of BN flip in the middle row as marked by down arrows.
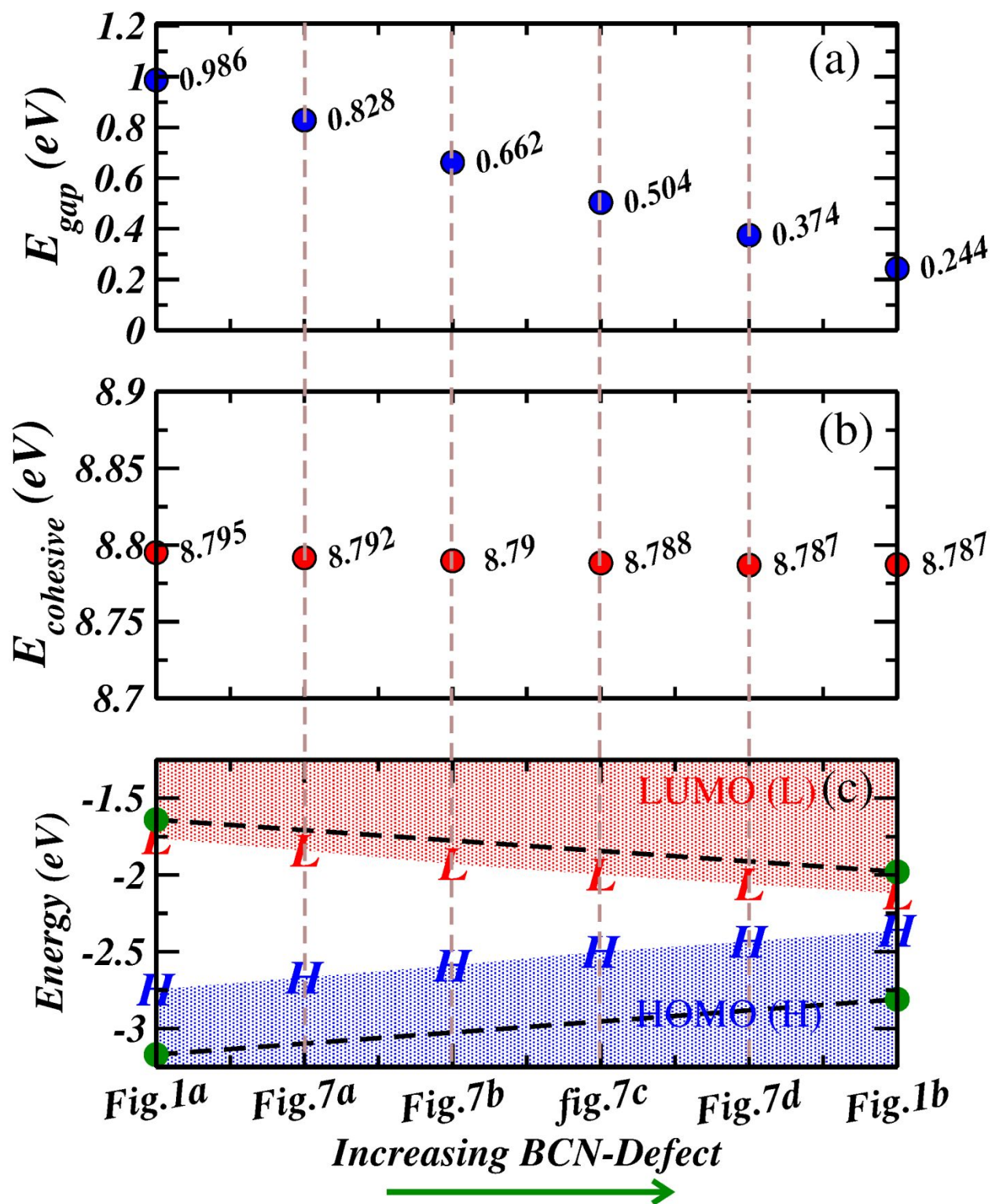
**Fig. 8** (a) Energy bandgap ($E_{gap}$), (b) Cohesive Energy ($E_{coh}$), and (c) HOMO-LUMO position (in eV) for BCN configurations given in Figure 1 and Figure 7. The black dashed line in (c) displays the band gap using the HSE functional. The points have been connected by lines to aid the eye and show the trend.
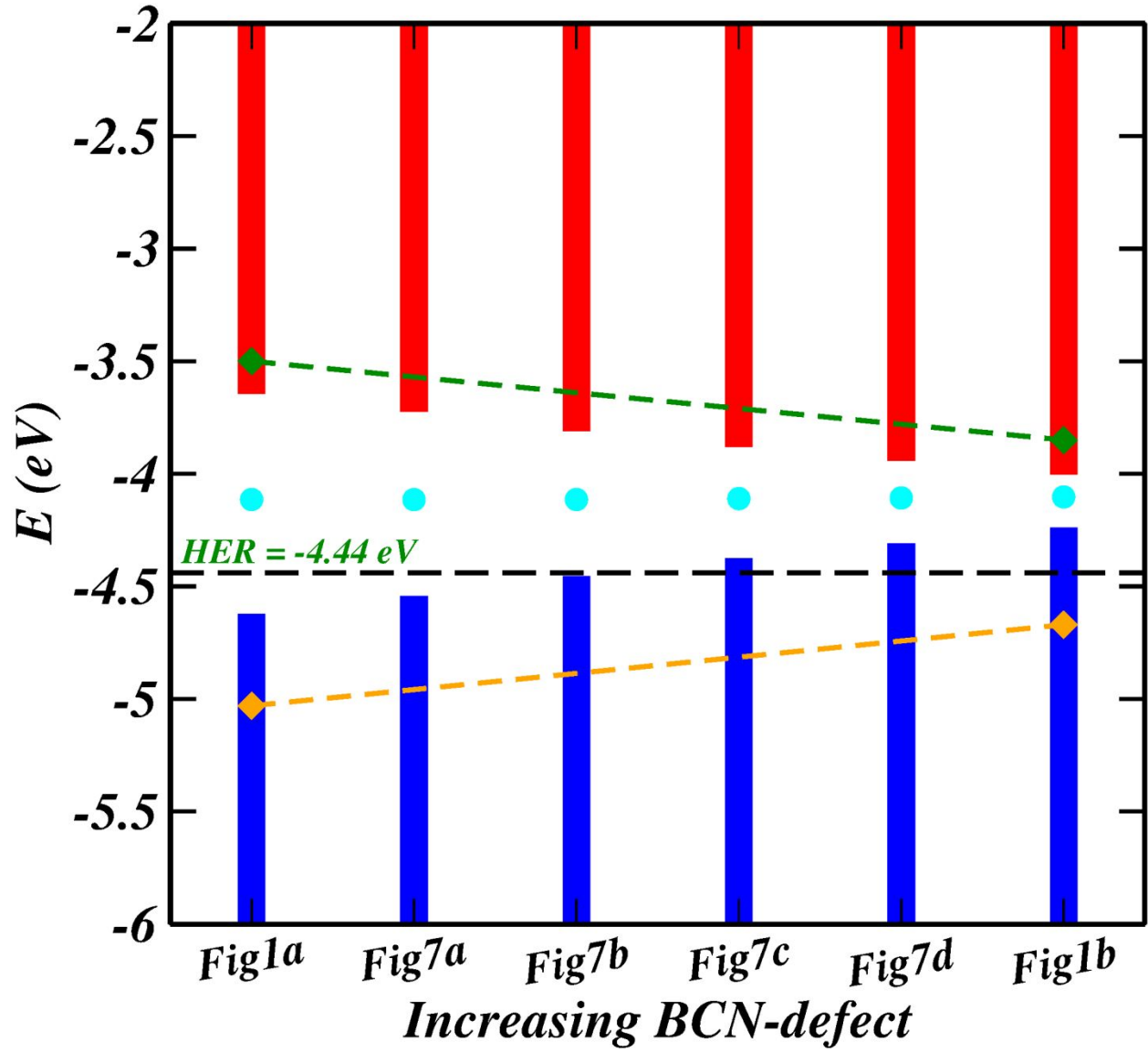
**Fig. 9** Band-edge energies of valence (blue) and conduction (red) band edges and Fermi energy (cyan circle) of the different configurations. The energy level for hydrogen evolution reaction (HER) is denoted by a dashed line. The orange (valence) and green (conduction) line denotes the band-edge positions using the HSE functional.

**Table 1** Deformation potential $E_1 (eV)$, elastic constant $C^{2D}{}_\beta$ $(N/m)$, carrier mobility μ $(10^4 cm^2 V^{-1} s^{-1})$ at 300 K for BCN and BCN-defect, respectively.

| Sheet | Carrier type | $E_1$ | $C^{2D}{}_\beta$ | $\mu$ |
|---|---|---|---|---|
| BCN | $h^x$ | 3.999 | 319.257 | 0.114 |
|  | $e^x$ | 4.540 | 319.257 | 0.117 |
| BCN | $h^y$ | 5.140 | 314.929 | 11.121 |
|  | $e^y$ | 3.086 | 314.929 | 3.188 |
| BCND | $h^x$ | 3.999 | 319.257 | 0.466 |
|  | $e^x$ | 4.540 | 319.257 | 0.309 |
| BCND | $h^y$ | 3.999 | 319.257 | 14.170 |
|  | $E^y$ | 4.540 | 319.257 | 9.383 |

**Table 2** Cohesive Energy, Formation Energy, HOMO and LUMO position, Bandgap for BCN and various configurations of BCN sheet.

| System | $E_{coh}$ (eV) | $E_{for}$ (eV) | HOMO | LUMO | $E_{gap}$ (eV) |
|---|---|---|---|---|---|
| Fig.1a | 8.795 | 0.259 | -2.746 | -1.760 | 0.986 |
| Fig.7a | 8.792 | 0.263 | -2.668 | -1.840 | 0.828 |
| Fig.7b | 8.790 | 0.264 | -2.580 | -1.925 | 0.654 |
| Fig.7c | 8.788 | 0.266 | -2.500 | -1.996 | 0.504 |
| Fig.7d | 8.787 | 0.267 | -2.433 | -2.059 | 0.375 |
| Fig.1b | 8.787 | 0.267 | -2.363 | -2.120 | 0.244 |

# References

1  C.N.R. Rao, K. Gopalakrishnan, A. Govindaraj, *Nano Today*, 2014 **9**, 324-343.

2  C.N.R. Rao, A.K. Sood, K.S. Subrahmanyam, A. Govindaraj, *Angew. Chem. Int. Ed.*, 2009, **48**, 7752-7777.

3  C.N.R. Rao, K.S. Subrahmanyam, H.S.S.R. Matte, B. Abdulhakeem, A. Govindaraj, D. Barun, K. Prashant, G. Anupama, J.L. Dattatray, *Sci. Technol. Adv. Mater.*, 2010, **11**, 54502-54519.

4  Z. Ye, H. Geng, X. Zheng, *Nanoscale Research Letters*, 2018, *13*, 376 (8pp).

5  S. Banerjee, S.K. Pati, *Nanoscale*, 2014, **6**, 13430-13434.

6  B-Y. Wang, H. Wang, L-Y. Chen et al., *Carbon*, 2016, **107**, 857-864.

7  P. Nath, S. Chowdhury, D. Sanyal, D. Jana, *Carbon*, 2014, **73**, 275-282.

8  C-K. Chang, S. Kataria, C-C. Kuo, A. Ganguli, B-Y. Wang, J-Y. Hwang, *ACS Nano*, 2013, **7**, 1333-1341.

9  M. Woinska, K.Z. Milowska, J.A. Majewski, *Phys. Status Solidi C*, 2013, **10**, 1167-1171.

10  A.V. Krasheninnikov, P.O. Lehtinen, A.S. Foster, P. Pyykko, R.M. Nieminen, *Phys. Rev. Lett.*, 2009, **102**, 126807 (4pp).

11  P.P. Shinde, V. Kumar, *Phys Rev B*, 2011, **84**, 125401 (6pp).

12  X.Fan,Z.Shen,A.Q.Liu,J-L.Kuo,*Nanoscale*,2012,**4**,2157-2165.

13  R. Zhao, J. Wang, M. Yang, Z. Liu, Z. Liu, *The Journal of Physical Chemistry C*,2012, **116**, 21098-21103.

14  K. Gopalakrishnan, A. Govindaraj, C.N.R. Rao, *J Mater. Chem. A*, 2013, **1**, 7563-7565.

15  W. Ding, Z. Wei, S. Chen, X. Qi, T. Yang, J. Hu, D. Wang, L.-J. Wan, S.F. Alvi, L. Li, *Angew. Chem. Int. Ed.*, 2013, **52**, 11755-11759.

16  Z.-S.Wu,W.Ren,L.Xu,F.Li,H.-M.Cheng,*ACSNano*, 2011, **5**, 5463-5471.

17  U. Maitra, U. Gupta, M. De, R. Datta, A. Govindaraj, C.N.R. Rao, *Angew. Chem. Int. Ed.*, 2013, **52**, 13057-13061.

18  L.S. Panchakarla, K.S. Subrahmanyam, S.K. Saha, A. Govin- daraj, H.R. Krishnamurthy, U.V. Waghmare, C.N.R. Rao, *Adv. Mater.*, 2009, **21**, 4726-4730.

19  I.Y. Jeon, Y.R. Shin, G.J. Sohn, H.J. Choi, S.Y. Bae, J. Mahmood, S.M. Jung, J.M. Seo, M.J. Kim, D. Wook Chang, L.Dai, J.B. Baek, *Proc. Natl. Acad. Sci. U. S. A.*, 2012, **109**, 5588- 5593.

20  I.Y. Jeon, H.J. Choi, M.J. Ju, I.T. Choi, K. Lim, J. Ko, H.K. Kim, J.C. Kim, J.J. Lee, D. Shin, S.M. Jung, J.M. Seo, M.J. Kim, N. Park, L. Dai, J.B. Baek, *Sci. Rep.*, 2013, **3**, 2260- 2265.

21  M. Cattelan, S. Agnoli, M. Favaro, D. Garoli, F. Romanato, M.Meneghetti, A. Barinov, P. Dudin, G. Granozzi, *Chem. Mater.*, 2013, **25**, 1490-1495.

22  H. Wang, Y. Zhou, D. Wu, L. Liao, S. Zhao, H. Peng, Z. Liu, *Small*, 2013, **9**, 1316-1320.

23  P. Rani, V. K. Jindal, *RSC Adv.*, 2013, **3**, 802-812.

24  M. Wu, C. Cao, J. Z. Jiang, *Nanotechnology*, 2010, **21**, 505202 (6pp).

25  S. Yang, L. Zhi, K. Tang, X. Feng, J. Maier, K. Mullen, *Adv. Funct. Mater.*, 2012, **22**, 3634-3640.

26  Z.-W. Liu, F. Peng, H.-J. Wang, H. Yu, W.-X. Zheng, J. Yang, *Angew. Chem. Int. Ed.*, 2011, **50**, 3257-3261.

27  T. Wu, H. Shen, L. Sun, B. Cheng, Liu, J. Shen, *New J. Chem.*, 2012, **36**, 1385-1391.

28  G. Bepete, D. Voiry, M. Chhowalla, Z. Chiguvare, N.J. Coville, *Nanoscale*, 2013, **5**, 6552-6557.

29  T.-W. Lin, C.-Y. Su, X.-Q. Zhang, W. Zhang, Y.-H. Lee, C.-W. Chu, H.-Y. Lin, M.-T. Chang, F.-R. Chen, L.-J. Li, *Small*, 2012, **8**, 1384-1391.

30  N. Kumar, K. Moses, K. Pramoda, S.N. Shirodkar, A.K. Mishra, U.V. Waghmare, A. Sundaresan, C.N.R. Rao, *J. Mater. Chem. A*, 2013, **1**, 5806-5821.

31  K. Gopalakrishnan, K. Moses, A. Govindaraj, C.N.R. Rao, *Solid State Commun.*, 2013, **175-176**, 43-50.

32  M. Chhetri, S. Maitra, H. Chakraborty, U.V. Waghmare, C.N.R. Rao, *Energy and Environmental Science*, 2016, **9 (1)**, 95-101.

33  K. Moses, V. Kiran, S. Sampath, C.N.R. Rao, *Chem. Asian J.*, 2014, **9 (3)**, 838-843.

34  S. Sen, K. Moses, A.J. Bhattacharyya, C.N.R. Rao, *Chem Asian J.*, 2014, **9**, 100-103.

35  U.A. Palnitkar, R.V. Kashid, M.A. More, D.S. Joag, L.S. Pan- chakarla, C.N.R. Rao, *Appl. Phys. Lett.*, 2010, **97**, 063102-063104.

36  R.B.Sharma, D.J.Late, D.S.Joag, A.Govindaraj, C.N.R.Rao, *Chem Phys. Lett.*, 2006, **428**, 102-108.

37  C. Huang, C. Chen, M. Zhang, L. Lin, X. Ye, S. Lin, M. An- tonietti, X. Wang, *Nature Communications*, 2015, **6**, 7698.

38  K. Maeda, K. Domen, *J. Phys. Chem. Lett.*, 2010, **1 (18)**, 2655-2661.

39  S.N. Shirodkar, U.V. Waghmare, T.S. Fisher, and Ricardo Grau-Crespo, *Phys. Chem. Chem. Phys.*, 2015, **17**, 13547- 13552.

40  V.K. Yadav, S.H. Mir, J.K. Singh, *Chem. Phys. Chem*, 2019, **20**, 687-694.

41  S.H. Mir, V.K. Yadav, J.K. Singh, *ACS Omega*, 2019, **4**, 3732- 3738.

42    C. Su et al. *Sci. Adv.*, 2019, **5**, eaav2252.

43 cp2k http://cp2k.berlios.de/.

44  J. VandeVondele, M. Krack, F. Mohamed, M. Parrinello, T. Chassaing, J. Hutter, *Comput. Phys. Commun.*, 2005, **167**, 103-128.

45  J. Perdew, K. Burke, M. Ernzerhof, *Phys. Rev. Lett.* 1996, **77**, 3865-3868.

46  S. Grimme, *J. Comput. Chem.*, 2006, **27**, 1787.

47  S. Grimme, J. Antony, S. Ehrlich, H. Krieg, *J. Chem. Phys.*, 2010, **132**, 154104.

48  J. VandeVondele, J. Hutter, *J. Chem. Phys.*, 2007, **127**, 114105.

49  G. Lippert, J. Hutter, M. Parrinello, *Molec. Phys.*, 1997, **92**, 477-487.

50  S. Goedecker, M. Teter, J. Hutter, *Phys. Rev. B*, 1996, **54**, 1703-1710.

51  C. Hartwigsen, S. Goedecker, J. Hutter, *Phys. Rev. B*, 1998, **58**, 3641-3662.

52  P. Giannozzi et al., *J. Phys. Condens. Mat.*, 2009, **21**, 395502.

53  A. M. Rappe, K.M. Rabe, E. Kaxiras, J.D. Joannopoulos, *Phys. Rev. B*, 1990, **41**, 1227.

54  H.J. Monkhorst, J. D. Pack, *Phys. Rev. B*, 1976, **13**, 5188.

55  P. Giannozzi, S.D. Gironcoli, P. Pavone, S. Baroni, *Phys. Rev. B*, 1991, **43(9)**, 7231-7242.

56  G. Madsen, D. Singh, *Comput. Phys. Commun.*, 2006, **175**, 6771.

57  L. A. Falkovsky, *Physics Letters A*, 2008, **372**, 5189-5192.

58  T. Li, C. He, W. Zhang, *Journal of Materials Chemistry A*, 2019, **70**, 4134-4144.

59  W. Shockley, J. Bardeen, *Phys. Rev.*, 1950, **77(3)**, 407-408.

60  J. Xi, M. Long, L. Tang, D. Wang, Z. Shuai, *Nanoscale*, 2012, **4(15)**, 4348-4369.

61  J. Qiao, X. Kong, Z.X. Hu, F.Yang, W. Ji, *Nature Communications*, 2014, **5**, 4475.

62  H. I. Rasool, C. Ophus, W. Klug, S Zettl, J. K. Gimzewski, *Nature Communications*, 2013, **4**, 2811.

63  B. Shevitski, M. Mecklenburg, W. A. Hubbard, E. R. White, B. Dawson, M.S. Lodge, M. Ishigami, B. C. Regan, *Phys Rev B Condens Matter Mater Phys.*, 2013, **87**, 045417.

64      M. Brehm, B. Kirchner, *J. Chem. Inf. Model.*, 2011, **51**, 2007-2023.

65 M. Thomas, M. Brehm, R. Fligg, P. Vohringer, B. Kirchner, *Phys. Chem. Chem. Phys.*, 2013, **15**, 6608-6622.

66 G. Lopez-Polina, M. Jaafar, F. Guinea, R. Roldan, C. Gomez-Navarro, J. Gomez-Herrero, *Carbon*, 2-17, **14**, 42-48.

67 A. Falin et. al, *Nature Communications*, 2017, **8**, 15815.

68  Q. Peng, W. Ji, S. De, *Computational Materials Science*, 2012, **56**, 11-17.

69 S. Azevedo, J R Kaschny, CMC de Castilho, F de Brito Mota, *Nanotechnology*, 2007, **18**, 495707.

70  J. Heyd, GE Scuseria, M. Ernzerhof, *J. Chem. Phys.*, 2003, **118**, 8207-8215.

71  C. Kittel, *Introduction to Solid State Physics, New York:John Wiley*, 1986, **6th Ed.**, 185.

72  J.-H. Kim, J. H. Hwang, J. Suh, S. Tongay, S. Kwon, C.C. Hwang, J. Wu, J. Young Park, *Applied Physics Letters*, 2013, **103 (17)**, 171604.

73  S.H. Mir, S. Chakraborty, J. Warna, S. Narayan, P. C. Jha, P. K. Jha, R. Ahuja, *Catalysis Science and Technology*, 2017, **7(3)**, 687-692.

74  S.Yu, H.D. Xiong, K. Eshun, H. Yuan, Q. Li, *Applied Surface Science*, 2015, **325**, 27-32.

75  N. Huo, Y. Yang,Y-N. Wu, X-G. Zhang, S.T. Pantelides, G. Konstantatos, *Nanoscale* ,2018, **10** ,15071-15077.

76  Electrical properties of silicon, Ioffe Institute Database, *http://www.ioffe.ru/SVA/NSM/Semicond/Si/electric.html*

77  C. Adamo, V. Barone, *J. Chem. Phys.*, 1999, **110(13)**, 6158-6170.

78  J.P. Perdew, Int. J. Quant. Chem., 1985, **28**, 497-523.

79  A. Pribram-Jones, D.A. Gross, K. Burke, *Annu Rev. Phys. Chem.*, 2015 **66**, 283-304.